Results in Physics 89 (2026) 108751

Contents lists available at ScienceDirect

Results in Physics

journal homepage: www.elsevier.com/locate/rinp

A novel geometric model of blood flow in stenosed small arteries with luminal surface irregularities

M.A. Elogail

General Education Department, Sharjah Maritime Academy (SMA), Sharjah, United Arab Emirates

ARTICLE INFO

Keywords:
Stenosis
Couple-stress fluid
Unit-step function
Wall shearstress
Endothelial surface irregularities

ABSTRACT

The main goal of this study is to develop a novel geometric model for blood flow in stenosed small arteries. Blood is represented as a couple stress fluid, and the effects of the luminal surface irregularities are explicitly incorporated. The model describes flow behavior upstream of, within, and downstream of the stenotic region. The problem's governing equations and the corresponding boundary conditions were set dimensionless via suitable quantities. The problem complexity was simplified, and closed-form analytical solutions were derived by carrying out the assumptions of lubrication approximation and low Reynolds number. This study presents an in-depth analysis to relate geometric parameters to hemodynamic variables (wall shear stress, pressure gradients). The significant role of pertinent parameters was displayed through plots. It has been noted that the small-scale stenotic surface irregularities superimpose high-frequency oscillations to the overall magnitude and shape of the pressure and shear stress profiles. Alignment of out-of-phase surface irregularities creates highly tortuous flow paths, whereas in-phase surface irregularities generate a single broad bell-shaped peak. The results provide mechanistic insight into the hemodynamic effects of luminal irregularities in stenotic lesions of small arteries. They may also contribute to future diagnostic and therapeutic approaches for arteriolosclerosis.

1. Introduction

Small arteries, typically a few hundred micrometers in diameter, are essential regulators of peripheral resistance and organ perfusion. They help in supplying oxygen and nutrient delivery to downstream microvascular networks [1,2]. The primary risk factors for small arteries disease include chronic hypertension, diabetes mellitus, advanced age, and smoking [3,4]. These factors induce endothelial dysfunction and chronic arterial wall injury [5], leading to arteriolosclerosis, lipohyalinosis, hyaline degeneration, and progressive stenosis of small penetrating arteries [6]. These pathological conditions disrupt the normally smooth vascular lumen surface, producing non-uniform wall thickening with an irregular interface with protrusions and micro-undulations [7]. Hemodynamics of stenosed arteries have been extensively investigated in the biofluid mechanics literature. Most previous studies have relied on simplified arterial geometries to represent luminal narrowing. Typical examples include bell-shaped stenosis models, represented in cosine-, Gaussian-, and parabolic-type forms [8–20], as well as elliptical/triangular/trapezoidal models [21–23] and multi-stenosis arrangements [24,25]. Although these models have yielded valuable insights into the relationship between stenosis severity and the hemodynamic quantities. They remain limited in their ability to represent complex lesion configurations. The present geometrical model offers a more general and physiologically realistic description of lesion morphology. It allows the upper and lower walls to be prescribed independently, thereby capturing true bilateral asymmetry. It further incorporates local wall irregularities through independently tunable parameters, so that mild and severe roughness can be imposed separately on each wall. In addition, phase parameters control the relative axial alignment of the opposing irregularities, permitting systematic examination of in-phase and out-of-phase configurations within the same framework. Finally, the connections between the stenotic lesion and the healthy lumen are enforced to be first-order differentiable by determining scaling constants from derivative-matching conditions at the lesion endpoints. Such C^1 continuity eliminates artificial slope discontinuities and contributes to stable analytical and numerical solutions. To the best of our knowledge, no previous study has simultaneously incorporated independent upper and lower wall profiles, explicit in-phase and out-of-phase wall alignment, tunable surface irregularities, and defined stenotic overlap regions within a single model. Together, these features enable the present formulation to capture geometric interaction effects that cannot be represented by earlier

E-mail address: mostafa.elogeil@sma.ac.ae.

https://doi.org/10.1016/j.rinp.2026.108751
Received 11 January 2026; Received in revised form 10 May 2026; Accepted 3 September 2026
Available online 7 September 2026
2211-3797/© 2026 The Author(s). Published by Elsevier B.V. This is an open access article under the CC BY license (http://creativecommons.org/licenses/by/4.0/).

idealized stenosis models.

While considerable research has focused on stenoses in large and medium-sized arteries, the hemodynamics of diseased microvascular structures have received comparatively less attention [26]. Blood flow in small arteries has distinctive characteristics that differ substantially from those in larger vessels [27,28]. Small arteries exhibit low Reynolds number, so flow is laminar. Small changes in the arterial radius cause large changes in resistance. Blood demonstrates significant non-Newtonian rheological characteristics in small blood vessels. The characteristic vessel dimension becomes comparable to the size of blood cells. Microscale rotational effects become non-negligible in these vessels . The couple-stress fluid model first proposed by Stokes [29] can capture the micro-rotation of blood cells and their interactions with surrounding structures [30]. Accordingly, this model is particularly appropriate for the microvessel-scale problem considered here. Unlike conventional shear-thinning models, which mainly account for shear-rate-dependent viscosity, or viscoelastic models, which represent elastic memory effects, the couple-stress formulation incorporates higher-order stresses associated with particle rotation. Some previous studies have demonstrated that couple-stress effects can profoundly affect pressure drops and wall shear stress distributions in stenotic vessels [31–35].

Cardiovascular diseases remain a leading cause of global mortality, accounting for approximately 31% of deaths worldwide according to the World Health Organization [26,36]. While atherosclerosis in large arteries has been extensively studied, arteriolosclerosis and lipohyalinosis in small penetrating arteries remain comparatively underexplored, despite their critical role in lacunar stroke and vascular dementia. Irregular stenosed lesions in small arteries can amplify local flow disturbances. They can also enhance energy dissipation across the stenotic region. In addition, they may generate abnormal wall shear stress at both the lesion site and downstream segments [37,38]. Even under nominally laminar, low-Reynolds-number conditions, such disturbances may promote endothelial dysfunction. They may also promote microthrombosis and downstream ischemia. Nonetheless, most existing studies have largely overlooked these geometric features in small arteries [39,40]. In their 2024 review, Hainsworth et al. [41] highlighted ongoing challenges in the definition, classification, and treatment of cerebral small vessel disease. These include the need for clearer diagnostic criteria, better subtyping in clinical trials, and more mechanism-based therapeutic approaches to arteriolosclerosis. In parallel, neuropathological assessment of brain arteriolosclerosis relies on semi-quantitative scales with only moderate inter-rater reliability [42]. Moreover, current in vivo imaging biomarkers do not provide a direct, neuropathology-equivalent readout of arteriolar wall pathology and its early functional consequences [43]. Together, these limitations underscore the need for mechanistic analytical models and, consequently, for geometric models that incorporate realistic stenosis morphology. It would be beneficial for these models to account for luminal surface irregularities under physiologically relevant conditions. Such models represent a valuable addition to literature. To address this gap, the current work introduces a new geometric model that captures overlapping asymmetric stenotic lesions and vessel wall irregularities with in-phase or out-of-phase shifts. The model is developed under small-Reynolds-number conditions and analyzed using the lubrication approximation to represent flow features characteristic of small arteries. In this context, the present analytical findings may help clarify the effects of lumen narrowing and geometric constraints, while also complementing imaging-based assessment and contributing to ongoing efforts to improve risk stratification in atherosclerotic disease.

The present study investigates the effect of endothelial surface irregularities in stenosed small arteries on key hemodynamic quantities, particularly the pressure gradient and the shear stress. Blood is modeled as a couple-stress fluid to capture its macroscopic and non-Newtonian characteristics. The complex geometric and topographical features of irregular stenotic luminal surfaces are constructed and controlled using a unit-step-function-based mathematical formulation. The novel geometrical model allows an asymmetric multi-scale wall morphology to be represented systematically as well as the lesion's surface roughness. This model offers a description that is more realistic and flexible than the smooth, idealized geometrical models that are traditionally used to describe atherosclerotic lesions.

2. Mathematical model

2.1. Geometric structure

In this study, a two-dimensional incompressible laminar blood flow through a microvessel of width 2 R_0. The vessel walls include overlapping stenosed lesion on the upper and lower walls of average length L_0. λ_1 and ξ_1 are the surface irregularities parameters for the upper and lower stenosed lesions, respectively. a and b represent the upper and lower amplitudes of the diseased wave-like shape endothelial lumen surface before and after the stenosis, respectively. A rectangle coordinate system is chosen where the $X-$ axis aligns with the direction of blood flow and the $Y-$ axis runs transverse to it. Fig. 1 displays the flow's geometry, while the mathematical description of the diseased microvessel wall geometry reads as follows:

Geometry of the upper wall

$$(\mathrm{U}[X]-\mathrm{U}[X-r_1])\left(R_0+a\sin(\frac{2\pi X}{L_0})\right),\ 0\le X\le r_1$$

$$W_1(X)=(\mathrm{U}[X-r_1]-\mathrm{U}[X-s_1])\left(\frac{\epsilon\Psi_1(X)}{R_0}\Psi_2(X)+\Psi_3(X)\right),r_1<X<s_1$$

$$(\mathrm{U}[X-s_1]-\mathrm{U}[X-z_1])\left(R_0+a\sin\left[\frac{2\pi X}{L_0}\right]\right),s_1\le X\le z_1.$$

With $\Psi_1(X)=\left(-\frac{1}{(r_1-s_1)^2}\left(-r_1{}^2R_0-2r_1s_1R_0+4h_1r_1s_1-s_1{}^2R_0-ar_1s_1\sin\left[\frac{2\pi r_1}{L_0}\right]-as_1{}^2\sin\left[\frac{2\pi r_1}{L_0}\right]-ar_1{}^2\sin\left[\frac{2\pi r_1}{L_0}\right]-ar_1s_1\sin\left[\frac{2\pi s_1}{L_0}\right]\right)+\left(-\frac{1}{(r_1-s_1)^2}(4r_1R_0-4h_1r_1+4s_1R_0-4h_1s_1+ar_1\sin\left[\frac{2\pi r_1}{L_0}\right]+3as_1\sin\left[\frac{2\pi r_1}{L_0}\right]+3ar_1\sin\left[\frac{2\pi s_1}{L_0}\right]+as_1\sin\left[\frac{2\pi s_1}{L_0}\right]\right)X+\left(-\frac{2}{(r_1-s_1)^2}\left(-2R_0+2h_1-a\sin\left[\frac{2\pi r_1}{L_0}\right]-a\sin\left[\frac{2\pi s_1}{L_0}\right]\right)\right)X^2\right),$

$$\Psi_2(X)=R_0\left(1+\lambda_1\sin\left[\frac{2\pi X}{L_0}\right]\right)$$

$$\Psi_3(X)=R_0\left(1-\epsilon\left(1+\lambda_1\sin\left(\frac{2\pi X}{L_0}\right)\right)\right)$$

Where r_1 and s_1 are the $x-$ coordinates of the start and end of the upper stenotic lesion. $\Omega_1(X)=\frac{\Psi_1(X)}{R_0}$ is a dimensionless parabolic shape function with vertex $(\frac{r_1+s_1}{2},\ h_1)$, and passes through (r_1,R_0) and (s_1,R_0). $\Psi_2(X)$ is a modulation function that creates waviness/roughness. The product $\frac{\Psi_1(X)}{R_0}\bullet\Psi_2(X)$ represents the upper stenotic lesion surface geometry $\Psi_3(X)$ acts as a transition function that ensures the continuity of $W_1(X)$ at $x=r_1$ and $x=s_1$.

Geometry of the lower wall

$$(\mathrm{U}[X]-\mathrm{U}[X-m_1])\left(-R_0-b\sin[\frac{2\pi X}{L_0}]\right),\ 0\le X\le m_1$$

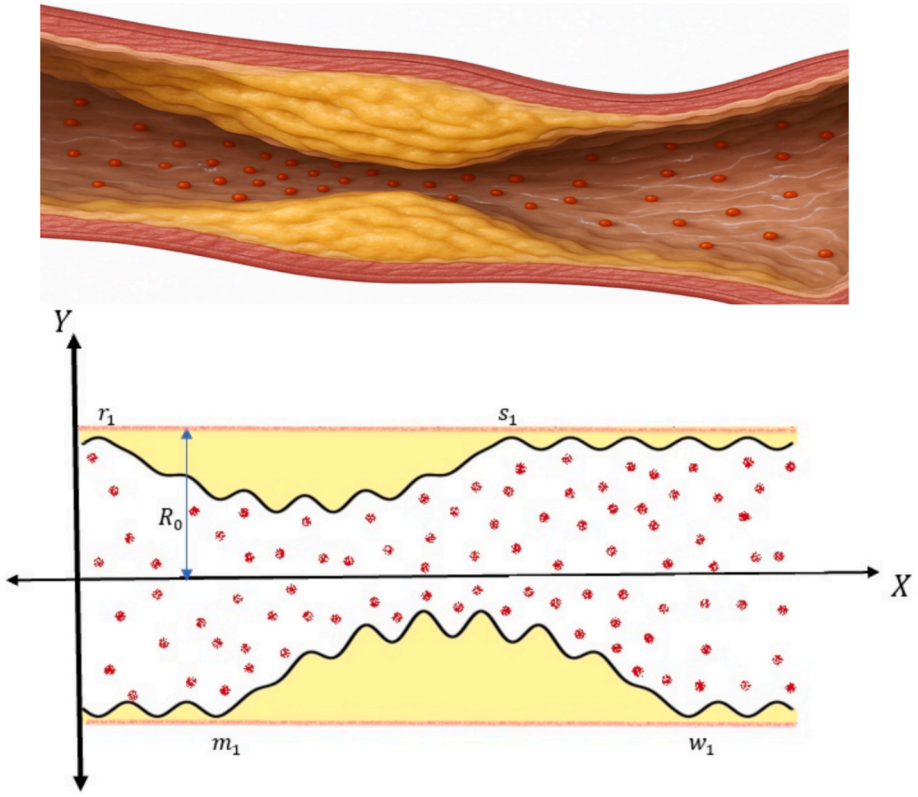

Fig. 1. 2D view of physical model of stenosed small artery.

$$W_2(X) = (\mathrm{U}[X-m_1]-\mathrm{U}[X-w_1])\left(\frac{\beta\Psi_4(X)}{R_0}\Psi_5(X)-\Psi_6(X)\right), m_1 < X < w_1$$

$$(\mathrm{U}[X-w_1]-\mathrm{U}[X-z_1])\left(-R_0-b\sin[\frac{2\pi X}{L_0}]\right), w_1 \le X \le z_1$$

$$\text{With } \Psi_4(X) = \left(-\frac{1}{(m_1-w_1)^2}\left(m_1{}^2R_0+2m_1w_1R_0+4g_1m_1w_1+w_1{}^2R_0+ bm_1w_1\sin\left[\frac{2m_1\pi}{L_0}\right]+bw_1{}^2\sin\left[\frac{2m_1\pi}{L_0}\right]+ bm_1{}^2\sin\left[\frac{2\pi w_1}{L_0}\right]+bm_1w_1\sin\left[\frac{2\pi w_1}{L_0}\right]\right)\right.$$
$$-\frac{1}{(m_1-w_1)^2}\left(-4m_1R_0-4g_1m_1-4w_1R_0-4g_1w_1-bm_1\sin\left[\frac{2m_1\pi}{L_0}\right]- 3bw_1\sin\left[\frac{2m_1\pi}{L_0}\right]-3bm_1\sin[2\pi w_1]- bw_1\sin[2\pi w_1]\right)X-\frac{2}{(m_1-w_1)^2}\left(2R_0+ 2g_1+b\sin\left[\frac{2\pi m_1}{L_0}\right]+b\sin\left[\frac{2\pi w_1}{L_0}\right]\right)X^2\Big),$$

$$\Psi_5(X) = R_0\left(1-\xi_1\sin[\frac{2\pi X}{L_0}]\right)$$

$$\Psi_6(X) = R_0\left(1-\beta\left(1-\xi_1\sin\left[\frac{2\pi X}{L_0}\right]\right)\right).$$

Where m_1 and w_1 are the $x-$ coordinates of the start and end of the lower stenotic lesion, $\Omega_2(X)=\frac{\Psi_4(X)}{R_0}$ is a dimensionless parabolic shape function with vertex $(\frac{m_1+w_1}{2}, g_1)$, and passes through $(m_1, -R_0)$ and $(w_1, -R_0)$. $\Psi_5(X)$ is a modulation function that creates waviness irregularities. The product $\frac{\Psi_4(X)}{R_0}\bullet\ \Psi_5(X)$ represents the lower stenotic lesion surface geometry . $\Psi_6(X)$ acts as a transition function that ensures the continuity of $W_2(X)$ at $x=m_1$ and $x=w_1$.

2.2. Governing equations

The problem modeling employs the mathematical model of the couple stress fluid for representing the non-Newtonian behavior of blood.

The governing equations are given by [44–46]

$$\frac{\partial U}{\partial X}+\frac{\partial V}{\partial Y}=0, \tag{1}$$

$$\rho\left(\frac{\partial U}{\partial T}+U\frac{\partial U}{\partial X}+V\frac{\partial U}{\partial Y}\right)=-\frac{\partial P}{\partial X}+\mu\left(\frac{\partial^2 U}{\partial X^2}+\frac{\partial^2 U}{\partial Y^2}\right)-\eta\left(\frac{\partial^4 U}{\partial X^4}+2\frac{\partial^4 U}{\partial X^2\partial Y^2}+\frac{\partial^4 U}{\partial Y^4}\right) \tag{2}$$

$$\rho\left(\frac{\partial V}{\partial T}+U\frac{\partial V}{\partial X}+V\frac{\partial V}{\partial Y}\right)=-\frac{\partial P}{\partial Y}+\mu\left(\frac{\partial^2 \mathrm{V}}{\partial X^2}+\frac{\partial^2 \mathrm{V}}{\partial Y^2}\right)-\eta\left(\frac{\partial^4 \mathrm{V}}{\partial X^4}+2\frac{\partial^4 \mathrm{V}}{\partial X^2\partial Y^2}+\frac{\partial^4 \mathrm{V}}{\partial Y^4}\right). \tag{3}$$

in which U, and V are the velocity components along X and Y of the arterial blood vessel respectively, t is the time, P is the pressure, ρ is the density, μ is the coefficient of viscosity of blood, and η is the couple stress viscosity.

The associated boundary conditions are given by

$$U=0,\ \frac{\partial^2 U}{\partial Y^2}=0,\ at\ Y=W_1 \tag{4a}$$

$$U=0,\ \frac{\partial^2 U}{\partial Y^2}=0,\ \ at\ Y=W_2 \tag{4b}$$

2.3. Dimensional analysis and approximations

Introducing the following non-dimensional quantities.

$$x=\frac{X}{L_0}, y=\frac{Y}{R_0}, u=\frac{U}{u_0}, v=\frac{V}{\delta u_0}, t=\frac{u_0}{L_0}T, \omega_1=\frac{W_1}{R_0}, \omega_2=\frac{W_2}{R_0}, \delta=\frac{R_0}{L_0}, a_1=\frac{a}{R_0}, a_2=\frac{b}{R_0}, P=\frac{R_0^2 p}{\mu c L_0}, h=\frac{h_1}{R_0}, g=\frac{g_1}{R_0}, m=\frac{m_1}{L_0}, w=\frac{w_1}{L_0}, r=\frac{r_1}{L_0}, s=\frac{s_1}{L_0}, R_e=\frac{\rho u_0 R_0}{\mu}, \gamma^2=\frac{\mu}{\eta}R_0^2. \tag{5}$$

Invoking the above non-dimensional quantities the governing equations in the non-dimensional form can be expressed as

$$R_e\delta\left(\frac{\partial u}{\partial t}+u\frac{\partial u}{\partial x}+v\frac{\partial u}{\partial y}\right)=-\frac{\partial p}{\partial x}+\delta^2\frac{\partial^2 u}{\partial x^2}+\frac{\partial^2 u}{\partial y^2}-\frac{1}{\gamma^2}\left(\delta^4\frac{\partial^4 u}{\partial x^4}+2\delta^2\frac{\partial^4 u}{\partial x^2\partial y^2}+\frac{\partial^4 u}{\partial y^4}\right) \tag{6}$$

$$R_e\delta^3\left(\frac{\partial v}{\partial t}+u\frac{\partial v}{\partial x}+v\frac{\partial v}{\partial y}\right)=-\frac{\partial p}{\partial y}+\delta^4\frac{\partial^2 v}{\partial x^2}+\delta^2\frac{\partial^2 v}{\partial y^2}-\frac{1}{\gamma^2}\left(\delta^6\frac{\partial^4 v}{\partial x^4}+2\delta^4\frac{\partial^4 v}{\partial x^2\partial y^2}+\delta^2\frac{\partial^4 v}{\partial y^4}\right) \tag{7}$$

Under the lubrication approximation, $\delta=\frac{R_0}{L_0}\ll 1$, and assuming low Reynolds number R_e, the governing eqs. (6)–(7) reduced to

$$0=-\frac{\partial p}{\partial x}+\frac{\partial^2 u}{\partial y^2}-\frac{1}{\gamma^2}\frac{\partial^4 u}{\partial y^4} \tag{8}$$

$$0=\frac{\partial p}{\partial y} \tag{9}$$

The lubrication parameter is defined using the stenosis length scale, since the dominant axial wall variation is localized within the constricted segment. Thus, we use $\delta=R_0/L_0$, where R_0 is the healthy-vessel radius and L_0 is the characteristic lesion length. Clinical coronary imaging reports lesion lengths several times the local lumen width corresponding to $\frac{L_0}{2R_0}\approx 5-9$ [47,48]. Pathological disease is also documented in sub-millimetre vessels, as cerebral small vessel disease includes arteriolosclerosis in penetrating arteries up to 300 μm in diameter [41]. Although direct lesion-length measurements below 1 mm are scarce, these data support the assumption that lesion axial extent remains several times the local lumen width, so that for arteries of width 50–500 μm, lesion lengths of order 10^{-1}–10^{0} mm to a few millimetres are reasonable, yielding $\delta\ll 1$.

The associated boundary conditions in non-dimensional form are:

$$u=0,\ \frac{\partial^2 u}{\partial y^2}=0\ at\ y=\omega_1 \tag{10a}$$

$$u=0,\ \frac{\partial^2 u}{\partial y^2}=0\ at\ y=\omega_2 \tag{10b}$$

The non-dimensional walls are as follows,

The upper wall

$$\omega_1=\begin{cases}(\mathrm{U}[x]-\mathrm{U}[x-\phi_1-r])(1+a_1\sin[2\pi(x-\phi_1)]), & 0\le x\le r\\ (\mathrm{U}[x-\phi_1-r]-\mathrm{U}[x-\phi_1-s])\psi_1(x), & r<x<s\\ (\mathrm{U}[x-\phi_1-s]-\mathrm{U}[x-\phi_1-z])(1+a_1\sin[2\pi(x-\phi_1)]), & s\le x\le z\end{cases}$$

The lower wall

$$\omega_2=\begin{cases}(\mathrm{U}[x]-\mathrm{U}[x-\phi_2-m])(-1-a_2\sin[2\pi(x-\phi_2)]), & 0\le x\le m\\ (\mathrm{U}[x-\phi_2-m]-\mathrm{U}[x-\phi_2-w])\psi_2(x), & m<x<w\\ (\mathrm{U}[x-\phi_2-w]-\mathrm{U}[x-\phi_2-z])(-1-a_2\sin[2\pi(x-\phi_2)]), & w\le x\le z\end{cases}$$

Where ϕ_1 and ϕ_2 are phase shifts in upper and lower walls respectively. r, s, m, and w, where chosen to satisfy the following conditions.

$r=\mathbb{N}_1+\frac{1}{2}, s=\mathbb{N}_2, m=\mathbb{N}_3+\frac{1}{2}, w=\mathbb{N}_4$ and $\mathbb{N}_1, \mathbb{N}_2, \mathbb{N}_3, \mathbb{N}_4$ are posi-

$$\text{With}\ \psi_1(x)=(\epsilon(\left(-\frac{1}{(r-s)^2}(-r^2-2rs+4hrs-s^2-a_1 rs\sin[2\pi r]-a_1 s^2\sin[2\pi r]-a_1 r^2\sin[2\pi s]-a_1 rs\sin[2\pi s])\right)+\left(-\frac{1}{(r-s)^2}(4r-4hr+4s-4hs+a_1 r\sin[2\pi r]+3a_1 s\sin[2\pi r]+3a_1 r\sin[2\pi s]+a_1 s\sin[2\pi s])\right)(x-\phi_1)+\left(-\frac{2}{(r-s)^2}(-2+2h-a_1\sin[2\pi r]-a_1\sin[2\pi s])\right)(x-\phi_1)^2)(1+\lambda_1\sin[2\pi(x-\phi_1)])+(1-\epsilon(1+\lambda_1\sin[2\pi(x-\phi_1)]))) \tag{11a}$$

$$\text{With}\ \psi_2(x)=\left(\beta\left(-\frac{1}{(m-w)^2}(m^2+2mw+4gmw+w^2+a_2 mw\sin[2m\pi]+a_2 w^2\sin[2m\pi]+a_2 m^2\sin[2\pi w]+a_2 mw\sin[2\pi w])-\frac{1}{(m-w)^2}(-4m-4gm-4w-4gw-a_2 m\sin[2m\pi]-3a_2 w\sin[2m\pi]-3a_2 m\sin[2\pi w]-a_2 w\sin[2\pi w])(x-\phi_2)-\frac{2}{(m-w)^2}(2+2g+a_2\sin[2m\pi]+a_2\sin[2w\pi])(x-\phi_2)^2\right)(1-\xi_1\sin[2\pi(x-\phi_2)])-(1-\beta(1-\xi_1\sin[2\pi(x-\phi_2)]))\right) \tag{11b}$$

tive integers, with $\mathbb{N}_2 > \mathbb{N}_1$,

$\mathbb{N}_4 > \mathbb{N}_3, |\mathbb{N}_4 - \mathbb{N}_1| > |\mathbb{N}_2 - \mathbb{N}_3| > 0$

ϵ and β are constants to be determined such that $\omega_1(x)$ and $\omega_2(x)$ are differentiable at the stenosis boundaries (To avoid divergence and ensure the accuracy and reliability of the solutions, differentiability at geometric junctions is a critical condition).

While the present analytical model assumes rigid vessel walls, this approximation is physiologically reasonable for diseased small arteries affected by cerebral small vessel disease and arteriolosclerotic remodeling. In such vessels, wall thickening, fibrotic remodeling, and extracellular matrix accumulation are associated with progressive vascular stiffening and reduced microvascular compliance [41,49–51].

3. Problem solution

The closed form solution of Eq. (8) is given by;

$$u(x,y) = \frac{C_1(x)\, e^{\gamma y} + C_2(x)\, e^{-\gamma y}}{\gamma^2} + C_3(x)\, y + C_4(x) + \frac{1}{2} y^2 \frac{dp}{dx}, \tag{12}$$

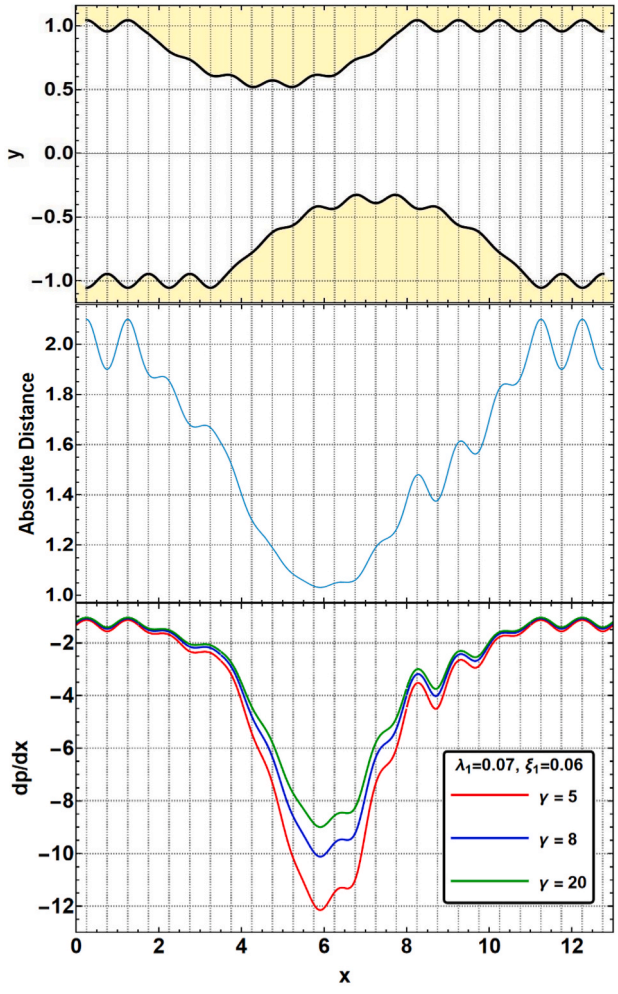

Fig. 2. Axial pressure gradient $\frac{dp}{dx}$ versus axial position x for various values of the couple-stress parameter γ, with $\phi_1 = 0$, $\phi_2 = 0$, $\lambda_1 = 0.07$, $\xi_1 = 0.06$, $r = 1.5$, $s = 8$, $m = 3.5$, $w = 11$, $q = 0.8$, $h = 0.05$, $g = -0.05$, $a_1 = 0.045$, $a_2 = 0.055$, $\epsilon = 0.48364$, $\beta = 0.6820563$, minimum lumen width = 1.031 at $x = 5.91$, Axial overlap 47.37%.

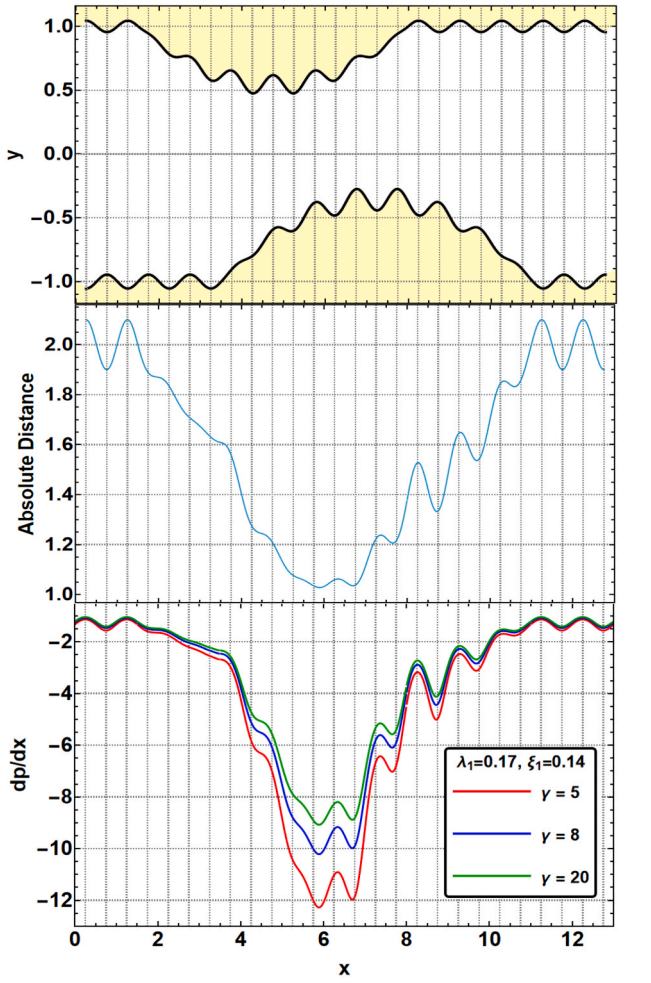

Fig. 3. Axial pressure gradient $\frac{dp}{dx}$ versus axial position x for various values of the couple-stress parameter γ, with $\phi_1 = 0$, $\phi_2 = 0$, $\lambda_1 = 0.17$, $\xi_1 = 0.14$, $r = 1.5$, $s = 8$, $m = 3.5$, $w = 11$, $q = 0.8$, $h = 0.05$, $g = -0.05$, $a_1 = 0.045$, $a_2 = 0.055$, $\epsilon = 0.48364$, $\beta = 0.6820563$, minimum lumen width = 1.028 at $x = 5.89$, Axial overlap 47.37%.

Where $C_1(x) = -\frac{1}{e^{\gamma h_1} + e^{\gamma h_2}} \frac{dp}{dx}$, $C_2(x) = -\frac{e^{\gamma(h_1+h_2)}}{e^{\gamma h_1} + e^{\gamma h_2}} \frac{dp}{dx}$,

$$C_3(x) = -\frac{1}{2}(h_1 + h_2)\frac{dp}{dx}, C_4(x) = \left(\frac{1}{\gamma^2} + \frac{1}{2} h_1 h_2\right)\frac{dp}{dx} \tag{13}$$

Applying boundary conditions (10a) and (10b), and Eq. (13), Eq. (12) becomes

$$u(x,y) = \frac{1}{2}\frac{dp}{dx}\left(y^2 + \frac{2}{\gamma^2} - \frac{2\mathrm{Cosh}\left[\frac{1}{2}\gamma(2y - h_1 - h_2)\right]\mathrm{sech}[\frac{1}{2}\gamma(h_1 - h_2)]}{\gamma^2} - y h_2 + h_1(-y + h_2)\right) \tag{14}$$

The mean flow

$$q = \int_{h_2}^{h_1} u(x,y)\, dy \tag{15}$$

Substituting Eq. (14) into Eq. (15) then integrating, we get

$$\frac{dp}{dx} = -\frac{12 q \gamma^3}{\gamma\left(-12 + \gamma^2 (h_1 - h_2)^2\right)(h_1 - h_2) + 24 \tanh[\frac{1}{2}\gamma(h_1 - h_2)]} \tag{16}$$

In the limit as $\gamma \to \infty$ (Newtonian fluid), and with $H(x) = h_1(x) - h_2(x)$

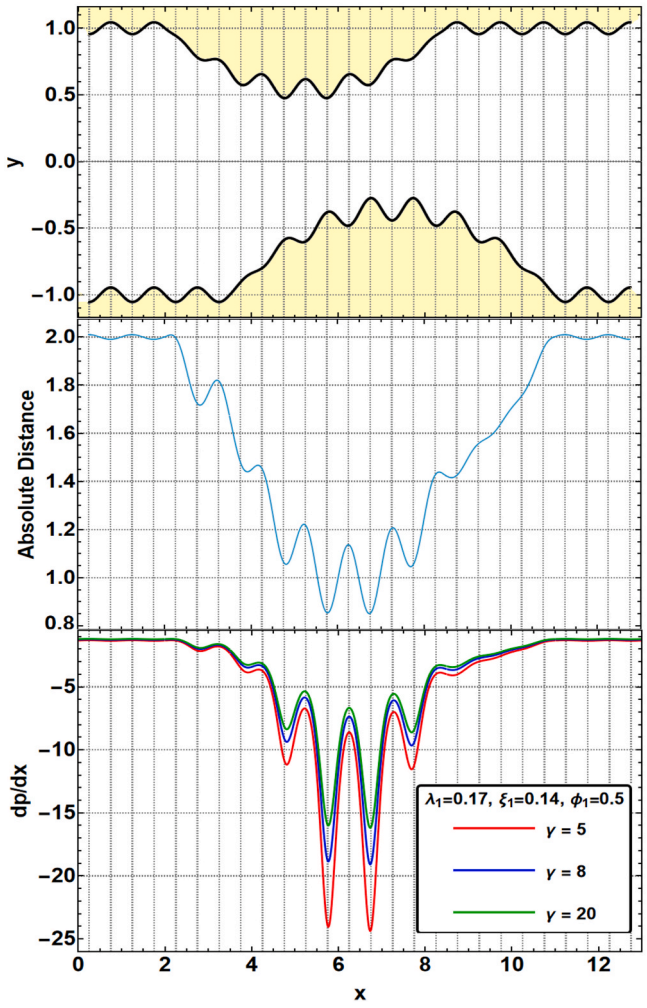

Fig. 4. Axial pressure gradient $\frac{dp}{dx}$ versus axial position x for various values of the couple-stress parameter γ, with $\phi_1 = 0.5$, $\phi_2 = 0$, $\lambda_1 = 0.17$, $\xi_1 = 0.14$, $r = 1.5$, $s = 8$, $m = 3.5$, $w = 11$, $q = 0.8$, $h = 0.05$, $g = -0.05$, $a_1 = 0.045$, $a_2 = 0.055$, $\epsilon = 0.48364$, $\beta = 0.6820563$, minimum lumen width = 0.85 at $x = 6.73$, Axial overlap 55.55%.

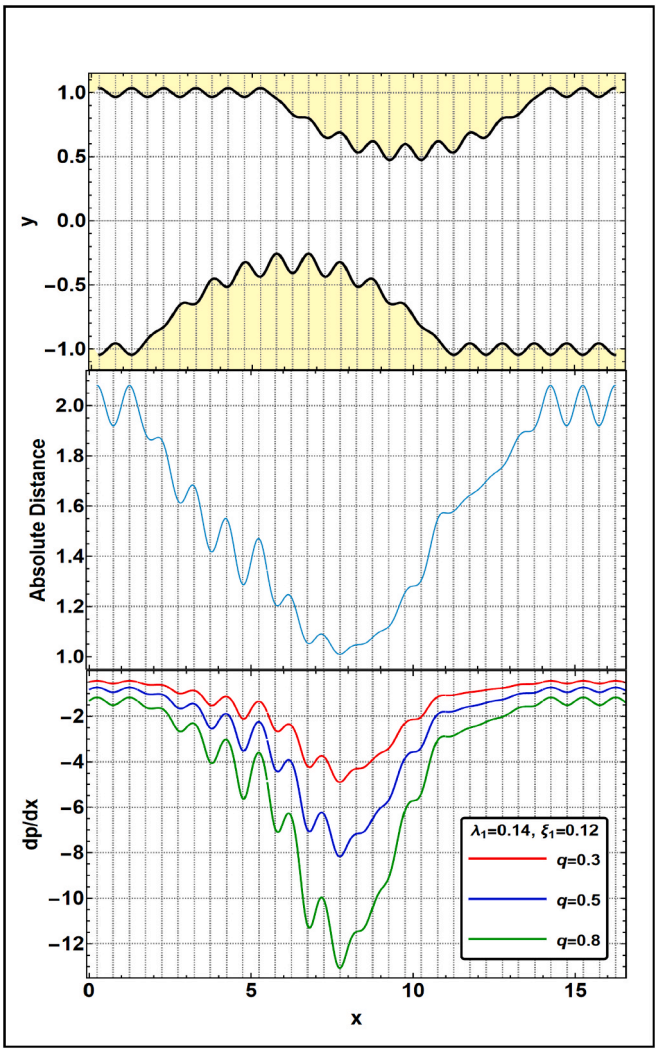

Fig. 5. Axial pressure gradient $\frac{dp}{dx}$ versus axial position x for various flow rates q, with $\phi_1 = 3$, $\phi_2 = -2$, $\lambda_1 = 0.14$, $\xi_1 = 0.12$, $r = 2.5$, $s = 11$, $m = 3.5$, $w = 13$, $\gamma = 5$, $h = 0.35$, $g = -0.15$, $a_1 = 0.035$, $a_2 = 0.045$, $\epsilon = 0.71894$, $\beta = 0.79002$, minimum lumen width = 1.001 at $x = 7.74$, Axial overlap 44%.

nearly constant. Eq. (16) reduces to the plane Poiseuille relation, $\frac{dp}{dx} \; -\frac{12q}{(h_1-h_2)^3}$[52]. In the present wavy, asymmetric channel with couple-stress effects, the effective resistance is larger than this classical value, particularly in regions where $H(x)$ is small.

The shear stress at the walls τ_w [47,53] is defined as,

$$\tau_w = \frac{\partial u}{\partial y} - \frac{1}{\gamma^2}\frac{\partial^3 u}{\partial y^3} \tag{17}$$

The pressure drop across the stenotic segment is defined as the pressure difference between the upstream and downstream ends of the constricted region,

$$\Delta p = -\int_{x_{in}}^{x_{out}} \frac{dp}{dx}\, dx \tag{18}$$

4. Results and discussions

Analytical solutions have been derived for the governing equations of couple stress fluid with the associated boundary conditions. The current work analyzes hemodynamics in microvessels using a geometric model that simulates stenosis with surface irregularities. Figs. 2–9 illustrate this analysis. Each figure has three panels. The top panel presents a cross-sectional view of a stenosed arterial segment featuring opposing superior and inferior lesions in axial overlap. Undulating geometry is observed along the arterial wall as well as superimposed upon the lesion surfaces, reflecting the topographical variations characteristic of pathological specimens. Vertical lines function as guides, spotlighting transitions in how the two sides of the opposing vessels' walls relate to each other. In some sections, the walls are "in-phase", indicating their peaks and troughs are aligned. In others, they are "out-of-phase", where a peak on one side aligns with a trough on the opposite side. The middle panel provides the absolute distance between the walls at each point along its length. The lower panel exhibits a chosen flow quantity throughout a range of selected parameters of interest. The vertical delineation lines extend through all the three panels, making it easy to see the correlation between geometric phase relationships, lumen width variations, and the resulting hemodynamic effects. This captures the complex, asymmetric luminal geometry characteristics of advanced atherosclerotic disease on blood flow features. The axial pressure gradient dp/dx and wall shear stress τ_w are essential factors in understanding blood flow dynamics within narrowed (stenosed) vessel segments. The pressure gradient measures the rate of pressure change along the vessel axis. In healthy, uniform vessels, the gradient is relatively small and negative, reflecting energy dissipated by minimal wall

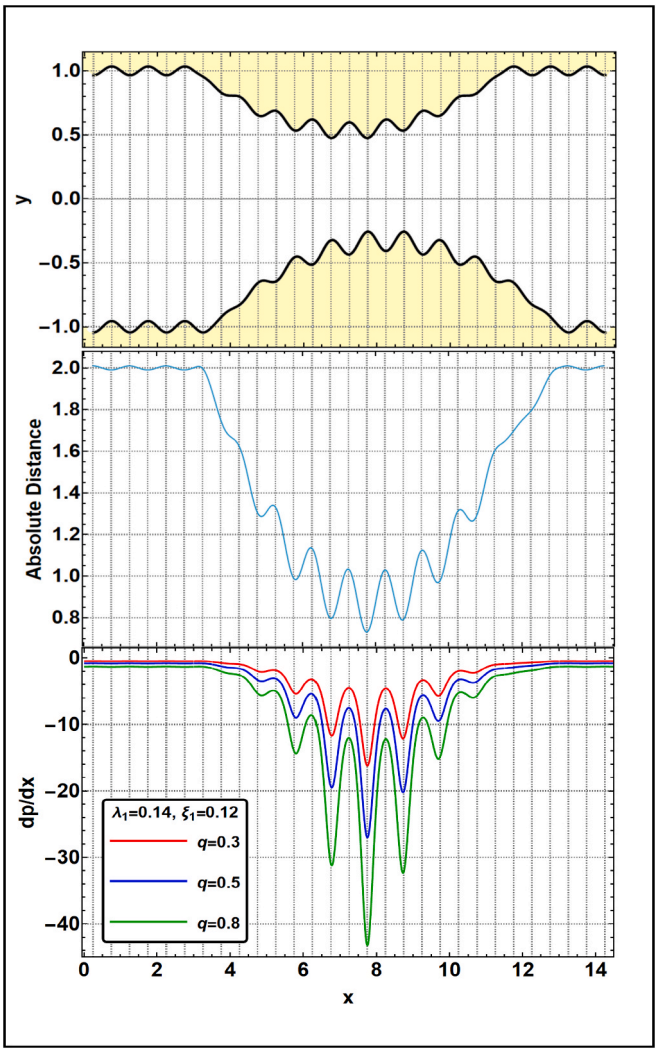

Fig. 6. Axial pressure gradient $\frac{dp}{dx}$ versus axial position x for various flow rates q, with $\phi_1 = 0.5$, $\phi_2 = 0$, $\lambda_1 = 0.14$, $\xi_1 = 0.12$, $r = 2.5$, $s = 11$, $m = 3.5$, $w = 13$, $\gamma = 5$, $h = 0.35$, $g = -0.15$, $a_1 = 0.035$, $a_2 = 0.045$, $\epsilon = 0.71894$, $\beta = 0.79002$, minimum lumen width $= 0.73$ at $x = 7.75$, Axial overlap 80%.

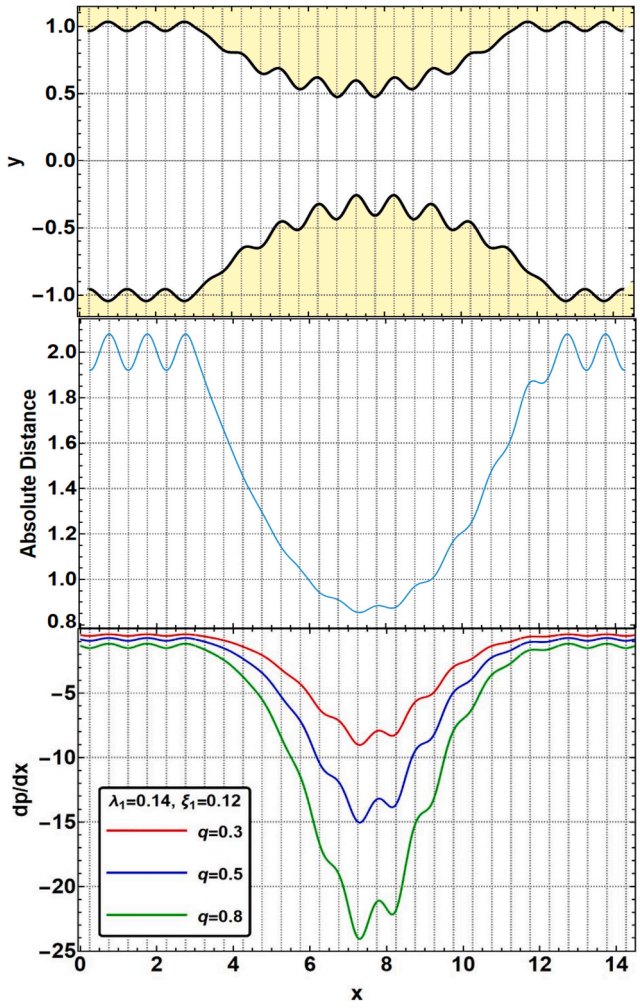

Fig. 7. Axial pressure gradient $\frac{dp}{dx}$ versus axial position x for various flow rates q, with $\phi_1 = 0.5$, $\phi_2 = -0.5$, $\lambda_1 = 0.14$, $\xi_1 = 0.12$, $r = 2.5$, $s = 11$, $m = 3.5$, $w = 13$, $\gamma = 5$, $h = 0.35$, $g = -0.15$, $a_1 = 0.035$, $a_2 = 0.045$, $\epsilon = 0.71894$, $\beta = 0.79002$, minimum lumen width $= 0.854$ at $x = 7.73$, Axial overlap 89.47%.

friction. Wall shear stress represents the tangential drag exerted by flowing blood on the vessel walls.

The couple-stress parameter $\gamma = R_0\sqrt{\mu/\eta} = R_0/l$, with $l = \sqrt{\eta/\mu}$ denoting the intrinsic microstructural length scale, is justified by blood's cellular composition. As reported by Secomb [54], RBCs are by volume the dominant suspended particles in blood. RBCs may therefore be regarded as the dominant microstructural elements relevant to couple-stress effects in small-artery hemodynamics. Fung [55] reported that the average human red cell diameter is $7.65 \pm 0.05\,\mu m$. Hence, for vessel diameters of 80-500 μm, corresponding to $R_0 \approx$ 40-250 μm, and taking $l \approx 8\,\mu m$ as a physiologically representative cellular length scale, the corresponding range of the couple-stress parameter is approximately $\gamma = R_0/l \approx$ 5-30. This is consistent with the range $\alpha =$ 5-25 employed by Srinivasacharya and Rao [56], where $\alpha = a\sqrt{\mu/\eta}$ is equivalent to the present definition of γ, thereby supporting the physiological plausibility of the parameter selections used in the current study, namely $\gamma = 5, 8, 20$.

The present study is formulated within the lubrication-approximation, low-Reynolds-number regime. In this context, the terms disturbed and oscillatory flow denote pronounced axial variations in pressure gradient and wall shear stress induced by geometric irregularities. They should not be interpreted as evidence of inertial instability, turbulence, or vortex formation.

4.1. Analysis of pressure gradient

The hemodynamic patterns depicted in Figs. 2-4 clarify how arterial geometry and wall phase alignment shape modulate the pressure–gradient distribution. Fig. 2 presents a case where the opposing lesions exhibit 47.37% overlaps along with the flow direction, with relatively mild irregularities ($\lambda_1 = 0.07$, $\xi_1 = 0.06$). The pressure gradient magnitude increases as the absolute distance to the stenotic throat decreases. Starting from values near -1 at an absolute distance of about 2.0 at the inlet, the pressure gradient decreases to approximately -12 when the distance is reduced to about 1.03 for $\gamma = 5$. The wide out-of-phase regions ($0 < x < 2.25$ and $8.25 < x < 13$), dp/dx exhibit moderate, high-frequency oscillations due to opposing wall undulations creating tortuous flow paths. While in the central in-phase stenotic region ($2.25 < x < 8.25$) the synchronized wall convergence produces a single, broad adverse gradient while maintaining gradual change in the gradient magnitude, reflecting the smooth shift in the lumen width. By increasing the lesion surface irregularities in Figure 2, we obtain Fig. 3 with ($\lambda_1 = 0.17$, $\xi_1 = 0.14$). While the overall shape of the pressure gradient curve is preserved, the magnitude of the pressure drop is greater due to increased frictional resistance, and more pronounced

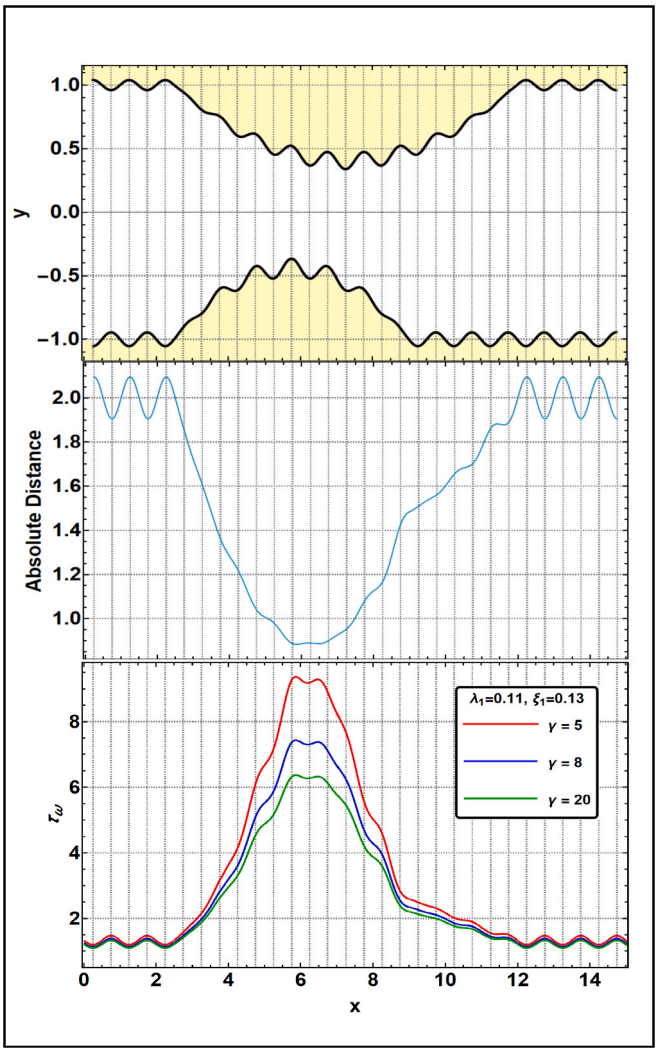

Fig. 8. Wall shear stress τ_w versus axial position x for various values of the couple-stress parameter γ, with $\phi_1 = 0$, $\phi_2 = 0$, $\lambda_1 = 0.11$, $\xi_1 = 0.13$, $r = 2.5$, $s = 12$, $m = 2.5$, $w = 9$, $q = 0.8$, $h = 0.25$, $g = -0.05$, $a_1 = 0.04$, $a_2 = 0.055$, $\epsilon = 0.79587$, $\beta = 0.591115$, minimum lumen width = 0.883 at $x = 5.866$, Axial overlap 68.42%.

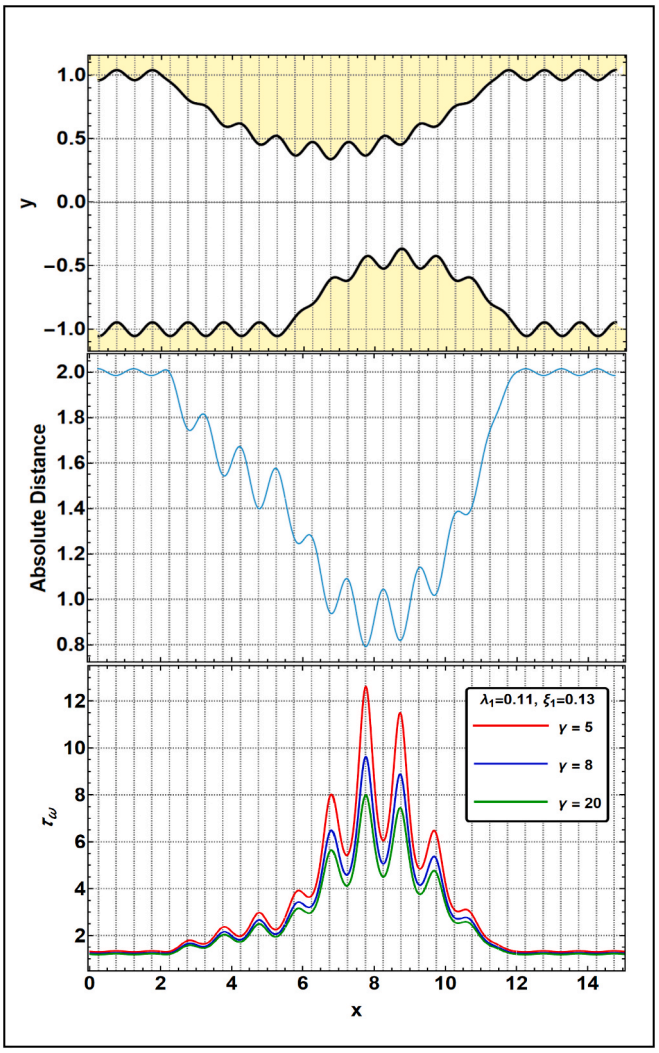

Fig. 9. Wall shear stress τ_w versus axial position x for various values of the couple-stress parameter γ, with $\phi_1 = -0.5$, $\phi_2 = 3$, $\lambda_1 = 0.11$, $\xi_1 = 0.13$, $r = 2.5$, $s = 12$, $m = 2.5$, $w = 9$, $q = 0.8$, $h = 0.25$, $g = -0.05$, $a_1 = 0.04$, $a_2 = 0.055$, $\epsilon = 0.79587$, $\beta = 0.591115$, minimum lumen width = 0.792 at $x = 7.76$, Axial overlap 60%.

oscillations are superimposed on the main curve, reflecting the heightened surface irregularity. A starkly different and more critical hemodynamic situation is presented in Fig. 4, which results from shifting the upper wall in Fig. 3 by half a unit to the right ($\phi_1 = 0.5$). This alteration increases the axial overlap to 55.55% and, critically, inverts the phase relationship so the central stenosed region ($2.75 < x < 8.75$) is now out-of-phase. The result is a narrow, tortuous path, with the minimum lumen width reduced to 0.85 (at $x \approx 6.73$). As blood flow is forced through this complex geometry, it undergoes pronounced local accelerations and decelerations dictated by the rapidly varying channel width. This generates a series of sharp, deep negative spikes in the pressure gradient, where magnitudes drop to as low as -24.36 at the throat for $\gamma = 5$. These spikes dominate the pressure–gradient profile and are a direct consequence of the enhanced viscous resistance in the highly confined, irregular luminal geometry. In contrast, the pressure gradient magnitude remains negligible in the wider, in-phase inlet and outlet regions ($0 < x < 2.75$ and $8.75 < x < 13$), where synchronized wall undulations and modest amplitude differences result in minimal oscillations. Figs. 2-4 consistently show that the pressure gradient becomes increasingly negative as the couple-stress effect is enhanced. This trend is most pronounced in the geometrically complex configuration of Fig. 4, where the out-of-phase geometry promotes pronounced spatial variations in the pressure field. The misaligned constrictions amplify the resistive forces from the couple-stress fluid, resulting in the sharp pressure gradient spikes observed. Each spike reflects the significant energy dissipation required to force the fluid through these narrow passages. Conversely, in the wider, more laminar regions, the couple-stress effect is minimal, clearly demonstrating its sensitivity of the fluid's rheological behavior to local geometric confinement.

Figures 5–7 examine how artery geometry affects the pressure gradient dp/dx at different flow rates q. All three figures use the stenotic lesion profile but vary the phase relationship and axial overlap. Fig. 5 shows a geometry with 44% axial overlap. The out-of-phase regions occur at $0 < x < 5.7$ and $13.75 < x < 16.25$, with a central in-phase region spanning $5.75 < x < 13.75$ where a minimum width of 1.001 occurs at $x = 7.74$. The pressure gradient scales nearly linearly with q throughout. In the tortuous but wide out-of-phase sections at the inlet and outlet, the gradient only oscillates mildly from -1 to -2 due to viscous wall friction. In stark contrast, the central in-phase region is dominated by a constriction that gives rise to a pronounced negative pressure gradient trough. The trough reaches depths of -8, -10, and -13 for $q = 0.3$, 0.5, and 0.8, respectively. Downstream of the throat, as

the vessel widens, the fluid decelerates. This deceleration initiates a sharp rise in the pressure gradient from its nadir, where the pressure gradient begins to rise from its nadir. The flow eventually re-stabilizes by $x > 13.75$, where the local pressure gradient returns to a baseline state. Nevertheless, while the pressure gradient stabilizes the significant pressure drop experienced within the stenosed region leads to irreversible energy losses. This energy, dissipated through viscous friction and the enhanced resistance imposed by the irregular geometry, is never regained, leaving the downstream flow with a permanent pressure deficit compared to the upstream condition. Fig. 6 presents a reversed phase relationship with axial overlap increased to 80%. The geometry is defined by in-phase sections at the ends ($0 < x < 3.25$ and $11.25 < x < 14.25$) and a central, critically narrow out-of-phase region ($3.25 < x < 11.25$). This central core, with a series of pronounced micro-stenoses and a minimum lumen width drastically reduced to 0.73 at $x = 7.75$, imposes severe geometric confinement on the flow. As blood flow is forced through this tortuous path it undergoes successive acceleration-deceleration cycles dictated by the rapidly varying local channel width. The hemodynamic consequence is the generation of exceptionally sharp and deep negative spikes in the pressure gradient, whose magnitudes intensify with flow rate to $-16, -27,$ and $-42,$ respectively, signifying extreme resistive forces. When blood approaches the narrowing it must accelerate in the upstream region, there must be a pressure drop ($dp/dx < 0$). This is the initial cause of the large negative dip in the gradient. The out-of-phase stenosis acts like an obstacle, promoting local pressure redistribution upstream. This redistribution can create a region of elevated pressure that results in a temporary adverse pressure gradient ($dp/dx > 0$), which pushes back against the incoming flow. This competition between acceleration and deceleration causes the oscillations observed upstream of the stenosis center. Downstream of the stenosis throat as the channel widens, the fluid exiting the throat decelerates. This conversion of kinetic energy back into potential energy initiates pressure recovery, creating a region of high pressure that results in a temporary adverse pressure gradient ($dp/dx > 0$). This recovery process is spatially varying. As the channel expands downstream of the throat, the geometric irregularities induce pronounced local variations in the pressure distribution. These variations create alternating favorable and adverse pressure-gradient segments. The pronounced downstream oscillations should therefore be interpreted as a consequence of geometric irregularity, strong confinement, and spatially varying viscous resistance. At low q, the flow is less energetic and more stable, leading to small oscillations. Conversely, at high q, the flow is more energetic and the geometric effects are amplified, producing larger-amplitude oscillations as clearly shown in the figure.

Fig. 7 presents a crucial comparison, featuring the highest axial overlap at 89.57% but reverting to a phase alignment as in Fig. 5. This setup has out-of-phase regions at the periphery ($0 < x < 3.25$ and $11.25 < x < 14.25$) and a central in-phase region ($3.25 < x < 11.25$) where the channel reaches its minimum width of 0.854 at $x = 7.3$. In the wider out of phase regions the opposing walls' waves create alternating, localized narrowings and widenings. Each local constriction causes a minor fluid acceleration (a dip in dp/dx), and each widening allows for a brief, partial pressure recovery (a rise in dp/dx). widening allows for a brief, partial pressure recovery (a rise in dp/dx).

However, since the overall channel is wide in this pre/post-stenotic zone, this region is characterized by low-amplitude, relatively high-frequency dp/dx oscillations around a slightly negative baseline.

Due to the synchronized wall geometry, the pressure gradient in the central stenotic core is defined by a broad, deep, U-shaped dp/dx bowl, rather than a series of sharp spikes. dp/dx becomes steeply negative, broadening and deepening to ≈ -25(for $q = 0.8$) as x approaches 7.3.

The complex "W" shape at the throat especially visible on the $q = 0.5$ and $q = 0.8$ curves is caused by the wall waviness (surface irregularities parameters λ_1 and ξ_1) being superimposed on the main stenotic curve. The in-phase waviness creates a local widening-narrowing cycles within the throat region, causing a momentary, localized deceleration (a slight rise in dp/dx) followed by another localized acceleration. Increasing the flow rate acts as an amplifier that deepens the main dp/dx valley, sharpens the "W" feature at the nadir, and increases the amplitude of the downstream oscillations, indicating a more pronounced geometrically induced variation in the hemodynamic response.

Across Figs. 1–7, the marked pressure drop across the stenosis reflects irreversible energy loss due to enhanced viscous dissipation within the geometrically irregular stenotic region. Even as the pressure gradient returns to its normal values downstream, the absolute pressure remains diminished [57]. This reduction weakens the driving pressure needed for the organs' perfusion. Blood supply metabolically active organs, including the kidneys, brain, and myocardium, is consequently threatened. Such deficits can precipitate compensatory flow redistribution or the vascular steal syndrome phenomenon [58]. To compensate for this energy loss, the heart is forced to generate higher pressures. This chronic strain increases cardiac hypertrophy and heightens the susceptibility to heart failure [59]. In tissues with limited regenerative capacity, persistent hypoperfusion causes cumulative damage. Clinically, such damage translates to symptoms such as exercise intolerance, angina, and cognitive impairment. Thus, the local stenosis of a vascular vessel imposes systematic consequences for cardiovascular structure and function.

4.2. Analysis of wall shear stress

Wall shear stress τ_w along the stenosed vessel arises from the combined influences of the wall geometry and the fluid properties. The primary dominant factor is the local lumen width. Fig. 8 illustrates a 68.42% axial extent of overlapped lesions and central in-phase constriction from $x = 2.75$ to $x = 11.75$ demonstrating a broad, bell-shaped peak in τ_w. The reduced cross-sectional area prior to the throat accelerates the flow until the shear stress reaches its maximum peak at the minimum arterial width 0.883 at $x \approx 5.866$. As the accelerated flow exits the narrow constriction, it suddenly enters the wider, lower-pressure region downstream. The rapid geometric expansion alters the local velocity profile significantly, resulting in a complex shear-stress distribution. In this zone, the vessel wall experiences gradually decreasing and oscillatory shear stress. These shear patterns are well known to be pro-inflammatory and damaging to the endothelial cells lining the vessel. They stimulate the endothelial cells to produce enzymes that progressively degrade elastin and collagen of the arterial wall. Over time, this persistent inflammatory and proteolytic activity weakens the wall. It may then dilate and form a localized micro-aneurysm. This aneurysmal segment represents a structurally compromised region that carries a substantial risk of rupture and life–threatening internal hemorrhage. In the wider regions $(0 < x < 2.75 \text{ and } 11.75 < x < 15)$, the wall geometry results in lower velocities and consequently, much lower average shear stress. This aneurysmal segment represents a structurally compromised region that carries a substantial risk of rupture and life–threatening internal hemorrhage.

In the wider regions $(0 < x < 2.75 \text{ and } 11.75 < x < 15)$, the wall geometry results in lower velocities and consequently, much lower average shear stress, while the different amplitudes of the opposite walls introduce a flow asymmetry that was enhanced with the out-of-phase wall geometry at these regions, ensuring an uneven distribution of these forces upon the superior and inferior endothelial surfaces. The regions of low and oscillatory shear stress, particularly in the pre- and post-stenotic zones, are known to be "athero-prone." This type of flow promotes the adhesion of inflammatory cells and the infiltration of LDL ("bad") cholesterol into the artery wall, which are the key steps in forming new arteriolosclerosis lesions or enlarging existing ones. The couple stress effect then acts as an overall amplifier: as γ decreases, the fluid's resistance to micro-rotation increases, raising τ_w across the entire domain. The large-scale constriction sets the overall form of the central peak, while the superimposed small-scale variations modulated by the

Table 1
Effect of couple-stress parameter γ on the maximum adverse pressure gradient, and total pressure drop across the stenotic interval for Figs. 2–4. Fixed geometry parameters are:$r = 1.5, s = 8, q = 0.8, h = 0.05, g = -0.05, a_1 = 0.045, a_2 = 0.055, m = 3.5, w = 11, \epsilon = 0.48364, \beta = 0.682056$.

	Irregularity Parameters	Axial Overlap	Minimum Distance	Stenoses Central Zone	Peak negative pressure gradient			Pressure Drop (Stenosis Interval)		
					$\gamma = 5$	$\gamma = 8$	$\gamma = 20$	$\gamma = 5$	$\gamma = 8$	$\gamma = 20$
Figure 2	$\lambda_1 = 0.07 \xi_1 = 0.06 \lambda_1 = 0.07 \xi_1 = 0.06$	$47.37\% \phi_1 = 0 \phi_2 = 0$	1.031at $x = 5.91$	In-phase	−12.15	−10.119	−8.996	49.337	42.882	39.297
Figure 3	$\lambda_1 = 0.17 \xi_1 = 0.14 \lambda_1 = 0.17 \xi_1 = 0.14$	$47.37\% \phi_1 = 0 \phi_2 = 0$	1.028 at $x = 5.89$	In-phase	−12.274	−10.214	−9.074	49.554	43.05	39.437
Figure 4	$\lambda_1 = 0.17 \xi_1 = 0.14 \lambda_1 = 0.17 \xi_1 = 0.14$	$55.55\% \phi_1 = 0.5 \phi_2 = 0$	0.85 at $x = 6.73$	Out-of-phase	−24.377	−19.094	−16.189	57.481	48.768	43.944

Table 2
Effect of flow rate q on the maximum adverse pressure gradient and total pressure drop across the stenotic interval for Figs. 5–7. Fixed geometry parameters are: $r = 2.5, s = 11, \gamma = 5, h = 0.35, g = -0.15, a_1 = 0.035, a_2 = 0.045, m = 3.5, w = 13, \epsilon = 0.71894, \beta = 0.79002$.

	Irregularity Parameters	Axial Overlap	Minimum Distance	Stenoses Central Zone	Peak negative pressure gradient			Pressure Drop (Stenosis Interval)		
					$q = 0.3$	$q = 0.5$	$q = 0.8$	$q = 0.3$	$q = 0.5$	$q = 0.8$
Figure 5	$\lambda_1 = 0.14 \xi_1 = 0.12 \lambda_1 = 0.14 \xi_1 = 0.12$	$44\% \phi_1 = 3 \phi_2 = -2$	1.001at $x = 7.74$	In-phase	−4.898	−8.164	−13.062	24.349	40.581	64.93
Figure 6	$\lambda_1 = 0.14 \xi_1 = 0.12 \lambda_1 = 0.14 \xi_1 = 0.12$	$80\% \phi_1 = 0 \phi_2 = 0$	0.73at $x = 7.75$	Out-of-phase	−16.222	−27.038	−43.261	36.966	61.611	98.577
Figure 7	$\lambda_1 = 0.14 \xi_1 = 0.12 \lambda_1 = 0.14 \xi_1 = 0.12$	$89.47\% \phi_1 = 0.5 \phi_2 = -0.5$	0.854at $x = 7.3$	In-phase	−9.027	−15.045	−24.072	35.139	58.565	93.704

Table 3
Effect of couple-stress parameter γ on the maximum wall shear stress and average wall shear stress over the stenotic interval for Figures 8 −9, Fixed geometry parameters are: $r = 2.5, s = 12, q = 0.8, h = 0.35, g = -0.05, a_1 = 0.04, a_2 = 0.055, m = 2.5, w = 9, \epsilon = 0.79587, \beta = 0.591115$.

	Irregularity Parameters	Axial Overlap	Minimum Distance	Stenoses Central Zone	Max Shear Stress			Average Shear stress (Stenosis Interval)		
					$\gamma = 5$	$\gamma = 8$	$\gamma = 20$	$\gamma = 5$	$\gamma = 8$	$\gamma = 20$
Fig. 8	$\lambda_1 = 0.11 \xi_1 = 0.13$	$68.42\% \phi_1 = 0.5 \phi_2 = 0$	0.883at $x = 5.866$	In-phase	9.366	7.433	6.368	4.421	3.727	3.241
Fig. 9	$\lambda_1 = 0.11 \xi_1 = 0.13$	$60\% \phi_1 = -0.5 \phi_2 = 3$	0.792at $x = 7.76$	Out-of-phase	12.613	9.625	7.987	4.159	3.521	3.168

surface undulations. These oscillations create a more potentially damaging hemodynamic environment for the endothelium than a smooth peak would do.

Based on Fig. 9, the wall shear stress (τ_w) profile is markedly different from the in-phase central case as seen in Fig. 8, demonstrating how the phase shift between plaques can alter the entire shear stress in the stenosed segment. In the wider peripheral in-phase regions ($0 < x < 2.25$ and $10.75 < x < 15$), the shear stress baseline attains lower levels showing very slight undulations superimposed on the primary flow profile. That is because the different amplitudes of the upper and lower wall irregularities create a flow asymmetry, which is partially damped by the in-phase geometry. The central out-of-phase region ($2.25 < x < 10.75$) with a roughly 60% luminal interface with a minimum wall–to–wall distance of about 0.792 at $x \approx 7.76$ presents the most critical hemodynamic scenario. This severe narrowing forces the fluid through a very confined channel and produces sharp, high magnitude oscillating shear stress spikes. Decreasing γ values (increasing the couple stress effect) further elevate the entire shear stress profile, but the amplification is most pronounced in the tight out-of-phase central region where velocity gradients are already high. In that region, strong and rapidly changing shear stress, together with the complex flow patterns induced by the irregular lesion surfaces, puts large mechanical loads on the endothelium. Chronic exposure to such abnormal shear patterns is well known to induce a pro-inflammatory endothelial phenotype, leading to increased production of proteolytic enzymes that degrade elastin and collagen within the vessel wall. Over time, this persistent inflammatory and proteolytic activity weakens the arterial wall, promoting post-stenotic dilation or the formation of microaneurysms localized out-pouchings that are structurally compromised and carry an increased risk of rupture and hemorrhage [60]. Even in the absence of dilation or rupture, regions of low and oscillatory shear stress especially in pre- and post-stenotic zones are prone to pathological remodeling. These shear environments promote endothelial dysfunction, inflammatory cell adhesion, and progressive intimal thickening or arteriolosclerosis, contributing to further narrowing and loss of the vessel health [61].

Tables 1–3 provide numerical support for the observations described above. Table 1 shows that Figs. 2 and 3 have the same geometric configuration: in-phase alignment within the stenotic overlap interval $x \in [3.5, 8.0]$(47.37%) and throat occlusion ~48.5%. They differ only in roughness amplitude. Their peak adverse pressure gradients and total pressure drops differ by less than 1% and 0.5% respectively, confirming the minor hemodynamic role of roughness amplitude under these conditions. Fig. 4, in contrast, has out-of-phase alignment within the stenotic overlap interval $x \in [3.5, 8.5]$(55.55%) and throat occlusion 57.5%. Relative to Fig. 3, it yields a maximum adverse pressure gradient approximately 99% higher and a total pressure drop approximately 16% higher, corresponding to a 17.3% increase in stenotic overlap interval extent and an 18.6% increase in throat occlusion. The throat minimum shifts downstream from $x_{\min} = 5.89$ to $x_{\min} = 6.73$. This downstream shift distributes the pressure load over a longer axial extent. It explains why the total pressure drop increase is moderate relative to the near-doubled of the peak gradient, a spatial distinction that total pressure

drop alone cannot capture.

Table 2 reveals that Fig. 5 has in-phase alignment within the stenotic overlap interval $x \in [5.5, 11.0]$(44%) and throat occlusion 50.0%. Fig. 7 has in-phase alignment within the stenotic overlap interval $x \in [3.0, 11.5]$(89.47%) and throat occlusion 57.3%. Relative to Fig. 5, Fig. 7 yields a maximum adverse pressure gradient approximately 84.3% higher and a total pressure drop approximately 44.3% higher, corresponding to a 103.34% increase in stenotic overlap interval extent and a 14.6% increase in throat occlusion within the same in-phase alignment class. Fig. 6, however, has out-of-phase alignment within the stenotic overlap interval $x \in [3.5, 11.5]$(80%) and throat occlusion 63.5%; relative to Fig. 5, it yields a maximum adverse pressure gradient approximately 231% higher and a total pressure drop approximately 51.8% higher. These results show that Fig. 6 exceeds Fig. 7 despite its narrower stenotic overlap interval (80% vs. 89.47%), indicating that out-of-phase alignment together with greater throat occlusion (63.5% vs. 57.3%) amplifies resistance more strongly than overlap extent alone. Although the present model is idealized, the results suggest that in complex arterial stenoses, lesion extent alone may not adequately represent functional severity, and that geometric features such as throat occlusion and the relative phase alignment of opposing wall irregularities may help explain why anatomically similar lesions can impose markedly different hemodynamic burdens.

Table 3 reveals a clear divergence between peak and spatially averaged wall shear stress. Fig. 8 has in-phase alignment within the stenotic overlap interval $x \in [2.5, 9.0]$(68.42%) and throat occlusion 55.9%. Fig. 9 has out-of-phase alignment within the stenotic overlap interval $x \in [5.5, 11.5]$(60%) and throat occlusion 60.4%. Despite the shorter overlap, Fig. 9 yields a peak wall shear stress approximately 34.7% higher than Fig. 8 at $\gamma = 5$(12.613 vs. 9.366), whereas the spatially averaged wall shear stress remains comparable (4.159 vs. 4.421, difference $\approx 5.9\%$). This indicates that the out-of-phase, more occluded geometry concentrates extreme shear loads at localized micro-constrictions rather than distributing them uniformly across the stenotic region. In small arteries, blood-cell rotational effects and the couple-stress mechanism intensify near-wall velocity gradients precisely at the narrowest cross-sections. The resulting concentration of peak wall shear stress at discrete micro-constrictions while the spatial mean remains comparable suggests that out-of-phase stenotic geometries may impose localized endothelial injury and microvessel remodeling disproportionate to what aggregate flow indices would indicate.

Since the present geometric model based on a unit-step-function formulation with surface irregularities, phase shifts, and asymmetric overlapping lesions is novel. A numerical comparison with prior studies is not feasible. The qualitative agreement with the established couple-stress and microvascular-flow studies supports the hemodynamic findings of the present results. The increase in pressure gradient and wall shear stress with stronger couple-stress effects is consistent with Sinha and Singh [62] and Srivastava [32]. Similar studies showed that tapering, constriction shape, and arterial bifurcation significantly modify impedance and wall shear stress [31,33,56]. The increase in pressure gradient with larger surface-irregularity amplitude is also consistent with Tripathi's amplitude-ratio results [30,63,64]. Finally, the adopted low-Reynolds-number framework is supported by microvascular-flow studies showing negligible inertial effects at comparable vessel scales [54,65]. Thus, the present model qualitatively reproduces established benchmark trends while extending them to irregular asymmetric stenoses. Furthermore, the exact recovery of the Poiseuille solution in the Newtonian limit ($\gamma \to \infty$) [52] confirms the mathematical correctness of the derived solution.

The results demonstrate that the hemodynamic burden in a stenosed small artery depends on several geometric factors. These include minimum lumen width, axial lesion overlap, surface irregularity amplitude, and the relative phase alignment of the opposing stenotic walls. Together, these geometric features control the pressure drop, wall shear stress distribution, and flow resistance across the stenotic region. If these geometric features are extracted from high-resolution imaging in future studies, the present analytical model could provide a first-order mechanistic basis for functional risk stratification. It could indicate whether a given lesion geometry is likely to produce excessive pressure loss or localized wall shear stress elevation. It could help estimate whether a lesion geometry is likely to cause excessive pressure loss or localized WSS elevation. This provides a mechanistic basis for future integration with image-based assessment, computational modelling, and clinical decision support.

5. Conclusions

The present study introduced a novel mathematical formulation that can simulate various stenosed microvessel structures with endothelial surface irregularities. Blood-like fluid was represented by the couple-stress model. The objective of the current study is to analyze the impact of the leading parameters on pressure gradient and wall shear stress through the stenosis. The main points and results are summarized below.

1. Employing the unit-step function adds a significant advancement in the mathematical simulation of vascular modeling considerably.
2. Stenosis with in-phase endothelial surface irregularities generates a single, broad, and predictable pressure gradient trough and a corresponding bell-shaped increase in wall shear stress.
3. Stenosis with out-of-phase endothelial surface irregularities creates a highly tortuous flow path and induces a hemodynamic regime characterized by multiple sharp spikes in the pressure gradient and high oscillatory peaks in wall shear stress.
4. In geometrically complex out-of-phase configurations, couple stress effects add extra resistance, which increases energy loss, enhances the pressure drop, and raises shear stress.
5. In geometrically simpler, in-phase stenotic flows, the impact of the couple-stress effect is modest.
6. In wider regions with more laminar flow, the couple stress effect is almost negligible, so it mostly matters in disturbed flow areas.
7. The surface irregularities add remarkable fluctuations to the overall pressure gradient and shear stress patterns, leading to more potential damage for the endothelium.
8. By ignoring vessel rugosity, smooth-wall simulations may underestimate the magnitude of hemodynamic variations linked to endothelial dysfunction and atherogenesis.
9. The shear stress peaks in out-of-phase stenoses suggest a potential mechanism for plaque rupture and subsequent thrombosis.
10. Low and oscillating shear stress in the regions pre- and post-stenotic zones align with conditions known to promote intimal thickening and pathological remodeling.

CRediT authorship contribution statement

The author confirms sole responsibility for the study conception and design, mathematical modeling and analysis, interpretation of results, and manuscript preparation. The author has read and approved the final manuscript.

Declaration of competing interest

The author declares that they have no known competing financial interests or personal relationships that could have appeared to influence the work reported in this paper.

Data availability

No data was used for the research described in the article.

References

[1] Aalkjær C, Nilsson H, De Mey JGR. Sympathetic and sensory-motor nerves in peripheral small arteries. Physiol Rev 2021;101:495–539. https://doi.org/10.1152/physrev.00007.2020.
[2] Mulvany MJ, Aalkjaer C. Structure and function of small arteries. Physiol Rev 1990;70:921–61. https://doi.org/10.1152/physrev.1990.70.4.921.
[3] Pantoni L. Cerebral small vessel disease: from pathogenesis and clinical characteristics to therapeutic challenges. Lancet Neurol 2010;9:689–701.
[4] Gao Y, Li D, Lin J, Thomas AM, Miao J, Chen D, et al. Cerebral small vessel disease: pathological mechanisms and potential therapeutic targets. Front Aging Neurosci 2022;14.
[5] Gutterman DD, Chabowski DS, Kadlec AO, Durand MJ, Freed JK, Ait-Aissa K, et al. The human microcirculation: regulation of flow and physiological responses. Circ Res 2016;118:157–72. https://doi.org/10.1161/CIRCRESAHA.115.305364.
[6] Schiffrin EL. Vascular remodeling in hypertension: mechanisms and treatment. Hypertension 2012;59:367–74.
[7] Mustapha N, Mandal PK, Johnston PR, Amin N. A numerical simulation of unsteady blood flow through multi-irregular arterial stenoses. App Math Model 2010;34:1559–73.
[8] Venkatesan J, Sankar DS, Hemalatha K, Yatim Y. Mathematical analysis of Casson fluid model for blood rheology in stenosed narrow arteries. J Appl Math 2013;2013:583809.
[9] Sriyab S. Mathematical analysis of non-Newtonian blood flow in stenosis narrow arteries. Comput Math Methods Med 2014;2014:479152.
[10] Owasit P, Sriyab S. Mathematical modeling of non-Newtonian fluid in arterial blood flow through various stenoses. Adv Differ Equ 2021;2021:340.
[11] Mahajan SS, Beleyur VS. Influence of serially developed two stenoses on flow characteristics of Jeffrey fluid flow through an artery. Cogent Eng 2025;12(1).
[12] Mandal D, Manna N, Chakrabarti S. Numerical study of blood flow through different double bell-shaped stenosed coronary artery during the progression of the disease, atherosclerosis. Int J Numer Meth Heat Fluid Flow 2010;20(6):670–98.
[13] Banerjee MK, Nag D, Ganguly R, Datta A. Hemodynamics in stenosed arteries—effects of stenosis shapes. Int J Comput Methods 2010;7(3):397–419.
[14] Kamangar S, Kalimuthu P, Govindaraju R, Badruddin IA, Badarudin A, Ahmed NJS, et al. Numerical investigation of the effect of stenosis geometry on the coronary diagnostic parameters. Sci World J 2014;2014:354946.
[15] Ausaru A, Nagarani P, Job VM. Numerical investigation of solute dispersion in a non-Newtonian fluid flow through a catheterized artery with mild stenosis. Chin J Phys 2024;89:541.
[16] Awad AM, Mekheimer KS, Elkilany SA, Zaher AZ. Leveraging elasticity of blood stenosis to detect the role of a non-Newtonian flow midst an arterial tube: Mazumdar and Keller models. Chin J Phys 2022;77:2520.
[17] Mashiku LR, Shaw S. Microgravity influenced unsteady dispersion during magnetic drug targeting in an inclined tumor-stenosed microvessel with slip effects. Chin J Phys 2024;92:915.
[18] Singh R, Sharma GC, Jain M. Mathematical modeling of blood flow in a stenosed artery under MHD effect through porous medium. IJE 2010;23:243.
[19] Ikbal MA, Chakravarty S, Wong KKL, Mazumdar J, Mandal PK. Unsteady response of non-Newtonian blood flow through a stenosed artery in magnetic field. J Comput Appl Math 2009;230:243.
[20] Misra JC, Shit GC. Blood flow through arteries in a pathological state: a theoretical study. Int J Eng Sci 2006;44:662.
[21] Liu X, Chen X, Zhang Y, Xie J, Jia X, Deng T, et al. The thermal behavior of blood flow in the arteries with various radii and various stenosis angles using non-Newtonian Sisko model. Alex Eng J 2022;61:7195.
[22] Kumar S, Kumar S. Blood flow with heat transfer through different geometries of stenotic arteries. Trends Sci 2023;20(8):6803.
[23] Kafle J, Subedi SS, Gautam PN. Delving into the impact of trapezoidal stenosis on hemodynamics. Appl Math E-Notes 2026;26:205–15.
[24] Khaliq S, Younas M, Abbas Z, Aljohani MA, Abualnaja KM. Thermally radiative flow of non-Newtonian Rabinowitsch fluid through a permeable artery with multiple stenoses of varying shapes. J Radiat Res Appl Sci 2025;18:101400.
[25] Shabbir MS, Ali N, Abbas Z. Unsteady blood flow of non-Newtonian fluid through a rigid artery in the presence of multi-irregular stenoses. J Braz Soc Mech Sci Eng 2018;40:413.
[26] Ziegler T, Abdel Rahman F, Jurisch V, Kupatt C. Atherosclerosis and the capillary network; pathophysiology and potential therapeutic strategies. Cells 2020;9:50.
[27] Cho YI, Cho DJ. Hemorheology and microvascular disorders. Korean Circ J 2011;41:287–95.
[28] Vahidkhah K, Balogh P, Bagchi P. Flow of red blood cells in stenosed microvessels. Sci Rep 2016;6:28194.
[29] Stokes VK. Couple stress in fluids. Phys Fluids 1966;9:1709–15.
[30] Tripathi D. Peristaltic flow of couple-stress conducting fluids through a porous channel: applications to blood flow in the micro-circulatory system. J Biol Syst 2011;19:461–77.
[31] Ponalagusamy R, Priyadharshini S. Couple stress fluid model for pulsatile flow of blood in a porous tapered arterial stenosis under magnetic field and periodic body acceleration. J Mech Med Biol 2017;17:1750109.
[32] Srivastava LM. Flow of couple stress fluid through stenotic blood vessels. J Biomech 1985;18:479–85.
[33] Ramana Reddy JV, Ha H, Sundar S. Modelling and simulation of fluid flow through stenosis and aneurysm blood vessel: a computational hemodynamic analysis. Comput Methods Biomech Biomed Eng 2023;26:1160–82.
[34] Reddy JVR, Srikanth D, Murthy SK. Mathematical modelling of couple stresses on fluid flow in constricted tapered artery in presence of slip velocity – effects of catheter. Appl Math Mech 2014;35:947–58.
[35] Prasad KM, Thulluri S, Phanikumari MV. Investigation of blood flow through an artery in the presence of overlapping stenosis. J Nav Archit Mar Eng 2017;14:39–46.
[36] World Health Organization. Cardiovascular diseases (CVDs). 2017.
[37] Yi J, Tian F-B, Simmons A, Barber T. Impact of modelling surface roughness in an arterial stenosis. Fluids 2022;7:179.
[38] Ekmejian AA, Carpenter HJ, Ciofani JL, Gray BHM, Allahwala UK, Ward M, et al. Advances in the computational assessment of disturbed coronary flow and wall shear stress: a contemporary review. J Am Heart Assoc 2024;13:e037129.
[39] Owen DG, Schenkel T, Shepherd DET, Espino DM. Assessment of surface roughness and blood rheology on local coronary haemodynamics: a multi-scale computational fluid dynamics study. J R Soc Interface 2020;17:20200327.
[40] Niu L, Qian M, Yang W, Meng L, Xiao Y, Wong KKL, et al. Surface roughness detection of arteries via texture analysis of ultrasound images for early diagnosis of atherosclerosis. PLoS One 2013;8:e76880.
[41] Hainsworth AH, Markus HS, Schneider JA. Cerebral small vessel disease, hypertension, and vascular contributions to cognitive impairment and dementia. Hypertension 2024;81(1):75–86.
[42] Lou JJ, Chang P, Nava KD, Chantaduly C, Wang HP, Yong WH, et al. Applying machine learning to assist in the morphometric assessment of brain arteriolosclerosis through automation. Free Neuropathol 2025;6:12.
[43] Blevins BL, Vinters HV, Love S, Wilcock DM, Grinberg LT, Schneider JA, et al. Brain arteriolosclerosis. Acta Neuropathol 2021;141(1):1–24.
[44] Tripathi D, Anwar BO. Transient magneto-peristaltic flow of couple stress biofluids: a magneto-hydrodynamical study on digestive transport phenomena. Math Biosci 2013;246:72–83.
[45] Ramesh K. Effects of slip and convective conditions on the peristaltic flow of couple stress fluid in an asymmetric channel through porous medium. Comput Methods Programs Biomed 2016;135:1.
[46] Ramesh K, Tripathi D, Anwar BO. Cilia-assisted hydromagnetic pumping of biorheological couple stress fluids. Propul Power Res 2019;8:221–33.
[47] Claessen BE, Smits PC, Kereiakes DJ, Parise H, Fahy M, Kedhi E, et al. Impact of lesion length and vessel size on clinical outcomes after percutaneous coronary intervention with everolimus- versus paclitaxel-eluting stents: pooled analysis from the SPIRIT (Clinical Evaluation of the XIENCE V Everolimus Eluting Coronary Stent System) and COMPARE (Second-generation everolimus-eluting and paclitaxel-eluting stents in real-life practice) randomized trials. J Am Coll Cardiol Intv 2011;4(11):1209–15.
[48] Price MJ, Saito S, Shlofmitz RA, Spriggs DJ, Attubato MJ, McLaurin BT, et al. First report of the Resolute Onyx 2.0-mm zotarolimus-eluting stent for the treatment of coronary lesions with very small reference vessel diameter. J Am Coll Cardiol Intv 2017;10(14):1381–8.
[49] Faraco G, Iadecola C. Hypertension: a harbinger of stroke and dementia. Hypertension 2013;62(5):810–7.
[50] Neltner JH, Abner EL, Baker S, Schmitt FA, Kryscio RJ, Jicha GA, et al. Arteriolar changes in the cerebral cortex and white matter in Alzheimer's disease and arteriolosclerosis. Brain 2014;137:255–67.
[51] Feihl F, Liaudet L, Waeber B. The macrocirculation and microcirculation of hypertension. Curr Hypertens Rep 2009;11:182–9.
[52] Bruus H. Theoretical microfluidics. Oxford University Press; 2008.
[53] Abu-Shaikha MF, Abbas Z, Rafiq M, Fayyaz AY. Influence of motility on couple stress fluid flow through a channel with slip constraints. Case Stud Therm Eng 2024;72:106234.
[54] Secomb TW. Blood flow in the microcirculation. Annu Rev Fluid Mech 2017;49:443–61.
[55] Fung YC, Tsang WCO, Patitucci P. High-resolution data on the geometry of red blood cells. Biorheology 1981;18:369–85.
[56] Srinivasacharya D, Madhava RG. Mathematical model for blood flow through a bifurcated artery using couple stress fluid. Math Biosci 2016;278:183–93.
[57] Binter C, Gotschy A, Sündermann SH, Frank M, Tanner FC, Lüscher TF, et al. Turbulent kinetic energy assessed by multipoint 4-dimensional flow magnetic resonance imaging provides additional information relative to echocardiography for the determination of aortic stenosis severity. Circ Cardiovasc Imaging 2017;10:e005486.
[58] Mirfakhraee M, Benzel EC, Guinto FC, et al. Unusual subclavian steal: bidirectional and antegrade blood flow in the vertebral artery. Neuroradiology 1995;37:503–11.
[59] Vancheri F, Longo G, Vancheri S, Henein M. Coronary microvascular dysfunction. J. Clin Med 2020;9:2880.
[60] Chiu J-J, Chien S. Effects of disturbed flow on vascular endothelium: pathophysiological basis and clinical perspectives. Physiol Rev 2011;91:327–87.
[61] Wu L-D, Shi Y, Kong C-H, et al. The GRK2/AP-1 signaling axis mediates vascular endothelial dysfunction and atherosclerosis induced by oscillatory low shear stress. Adv Sci 2025;12:e01981.
[62] Sinha P, Singh C. Effects of couple stresses on the blood flow through an artery with mild stenosis. Biorheology 1984;21:303–15.
[63] Tripathi D. Peristaltic hemodynamic flow of couple-stress fluids through a porous medium with slip effect. Transp Porous Media 2012;92:559–72.
[64] Maiti S, Misra JC. Peristaltic transport of a couple stress fluid: some applications to hemodynamics. J Mech Med Biol 2012;12:1250048.
[65] Pindera MZ, Ding H, Athavale MM, Chen Z. Accuracy of 1D microvascular flow models in the limit of low Reynolds numbers. Microvasc Res 2009;77:273–80.